Carbohydrate Polymers 285 (2022) 119209

Contents lists available at ScienceDirect

Carbohydrate Polymers

journal homepage: www.elsevier.com/locate/carbpol

Chitosan for constructing stable polymer-inorganic suspensions and multifunctional membranes for wound healing

Liangyu Wang [a], Lin Du [b], Mengmeng Wang [a], Xing Wang [a], Saihua Tian [a], Yan Chen [a], Xiaoyue Wang [b], Jie Zhang [b,*], Jun Nie [a], Guiping Ma [a,*]

[a] Beijing Laboratory of Biomedical Materials, Ministry of Education, Beijing University of Chemical Technology, Beijing 100029, PR China
[b] Department of Gastroenterology, Beijing Anzhen Hospital, Capital Medical University, Beijing 100029, China

ARTICLE INFO

Keywords:
Chitosan
Sugar coating
Molecular needles
Humidity sensing
Infectious wounds therapy

ABSTRACT

Restricted by the rigid chain structure, chitosan-based materials are very fragile and easy to break up. Herein, a stable and positively charged chitosan/$Ti_3C_2T_x$ suspension was successfully constructed by adjusting mixing sequence, pH and ratio of chitosan to $Ti_3C_2T_x$ to prepare a multifunctional membrane (P-CM) with self-standing ability, good flexibility, biocompatibility, excellent photothermal antibacterial properties, and sensitive humidity sensing properties. In the first stage, protonated chitosan acted as sugar coatings was able to be encapsulated on the surface of $Ti_3C_2T_x$ nanosheets by electrostatic self-assembly, in turn achieving charge reversal of the nanoparticles. In the second stage, chitosan acted as molecular needles to suture the membrane formed by chitosan/$Ti_3C_2T_x$ particles via vacuum filtration (VAF) with the commercial flexible poly(vinylidene fluoride) (PVDF) membrane. The as-prepared P-CM membrane simultaneously solves the problem of insufficient flexibility of a single component chitosan membrane and the poor bonding between pure $Ti_3C_2T_x$ membranes and substrate membrane.

1. Introduction

Globally, more than half of the emerging infectious diseases (EIDs) are caused by bacterial pathogens, which imposes a severe burden on global economics and public health security (Gupta et al., 2019; Shao et al., 2021; Xin et al., 2019). Meanwhile, due to the increasing resistance of bacteria to antibiotics through de novo mutation and the limited development of effective antibacterial agents, exacerbation of skin wounds induced by bacterial infection is becoming a serious potential threat to patients' health (Brown & Wright, 2016; Jones et al., 2008; Wang et al., 2019). Targeting the problem of drug-resistance of bacteria, one of the current solutions is to combine multiple active antibiotics to treat disease. However, this treatment modality also has significant pitfalls: limited by the clinical experience, wide interindividual variation in efficacy, unknown side effects and so on. Therefore, it is of great importance and urgency to seek effective antibacterial agents that do not cause increased resistance of bacteria. Over a long period in the past, the antimicrobial activities as well as mechanism of inorganic nanomaterials such as metal nanoparticles (NPs), semiconductor NPs, and carbon-based nanomaterials has been an exploration focus due to their nonspecific bactericidal effect (Xin et al., 2019). It has been reported that the combination of different nanomaterials can produce superior antibacterial effect. S. Nayak et al. studied the antibacterial level of graphene oxide (GO) deposited on different metal substrates and found that benefitting from nonoxidative and ROS-mediated oxidative stress mechanism, GO-metals system has much stronger antibacterial ability than single GO system, which further expands the potential use of inorganic nanomaterials in biomedical areas (Panda et al., 2018).

In the past decades, "MXenes", a new family of two-dimensional (2D) organic nanomaterials, where "M" represents early transition metal and "X" represents carbon and/or nitrogen element, has received extensive attention from researchers in the fields of electricity, heat, optics, electromagnetics, sensing, biomedicine and so on (Dong et al., 2020; Tao et al., 2019; Yang, Wang, et al., 2018; Jiang et al., 2020). Among the MXenes family, $Ti_3C_2T_x$ MXene is the most studied ones. The existence of terminal functional groups such as —OH, —O, or —F endows the $Ti_3C_2T_x$ MXene nanosheets with good hydrophilicity and electronegative surface, which can make them stably disperse in aqueous solution without the addition of dispersant (Jin et al., 2021; Maleski et al., 2017). Recently, several studies about the antibacterial activity of MXenes have

* Corresponding authors.
E-mail addresses: zhangjie4155@sina.com (J. Zhang), magp@mail.buct.edu.cn (G. Ma).

https://doi.org/10.1016/j.carbpol.2022.119209
Received 20 September 2021; Received in revised form 10 January 2022; Accepted 31 January 2022
Available online 4 February 2022

been reported. For example, Y. Gogotsi et al. tested in detail the antibacterial activity of single- and few-layer $Ti_3C_2T_x$ (FL-$Ti_3C_2T_x$) MXene nanosheets in the form of colloidal solution against gram-positive bacteria *Bacillus subtilis* (*B. subtilis*) and gram-negative bacteria *E. coli* (Rasool et al., 2016). The results showed an excellent dose-dependent antibacterial property of $Ti_3C_2T_x$ MXene in colloidal solution both against *B. subtilis* and *E. coli*. In addition, MXenes materials have become a research hotspot in the field of photothermal therapy (PTT) owing to the excellent photothermal effect (Han et al., 2018; Lin et al., 2018). Hong et al. systematically investigated the photothermal antibacterial ability of MXene under different conditions (e.g. types of MXenes and bacteria, concentration of MXenes, light wavenumber, light intensity, light time), eventually demonstrating a rapid and broad-spectrum photothermal antibacterial activity of MXenes (Wu et al., 2020). The above studies further expand the theoretical basis for the application of MXenes materials in biomedical applications.

Nevertheless, when MXenes are applied to the human in vivo environment, the side effects such as systemic or local toxicity remains a serious concern and their long-term biocompatibility in vivo should be paid more attention. To further improve the biosafety of MXenes and enlarge their applications in biomedical areas, Modifying MXenes or preparing MXenes-based nanocomposite products are two well-established strategies. Shi et al. obtained the surface modified products of $Ti_3C_2T_x$ MXene ($Ti_3C_2T_x$-SP) using soybean phospholipid to encapsulate $Ti_3C_2T_x$ nanosheets (Lin et al., 2017). The modified $Ti_3C_2T_x$-SP exhibited better biocompatibility and less toxicity, and more suitable for application in biological fields. Considering the biosafety as well as the bio functionality (e.g. antibacterial, hemostatic, and pro-healing properties) (Lord et al., 2011; Ren et al., 2020; Xu, Guo, et al., 2018; Liang et al., 2019) of natural polymers within the biological fields, macromolecules such as cellulose, sodium alginate, and chitosan are used to construct organic-inorganic composite system (Jiang et al., 2021) through covalent binding (static covalent bonds or dynamic covalent bonds) or noncovalent interactions (e.g. van der Waals forces, hydrogen bonding, hydrophobic or electrostatic interactions).

To date, chitosan, the deacetylation product of chitin, the only basic polysaccharides among natural polysaccharides, has been proved to possess good biodegradability, cell affinity, and biological functions such as antibiosis, hemostasis, and healing promoting, which make it an ideal biomaterial for biomedical applications (Ma et al., 2021; Zhao et al., 2018). chitosan can dissolve in an acidic environment by protonation of amine groups ($—NH_2 \rightarrow —NH_3^+$), and thus forming randomly dispersed molecular chains with positively charges (Wang, Zhong, et al., 2020). Benefitting from the hydrophilic advantage of MXene, it has become a common method to prepare various MXene-polymer composites (such as MXene-cellulose, MXene-alginate, MXene-PVA or MXene-chitosan composites) (Zhang et al., 2019; Zhang, Cheng, et al., 2020; Luo et al., 2021; Xu, Liu, et al., 2018) via hydrogen bonding self-assembly as well as electrostatic self-assembly in aqueous systems. However, the stability of suspension formed by MXene with polymers has rarely been reported in detail. Especially for protonated chitosan, strong electrostatic interactions would induce composite nanoparticles formed by MXene and chitosan sedimentation in suspension thus causing a failure to form a stable homogeneous system. Therefore, it is still necessary to explore the underlying conditions for the formation of stable MXene/chitosan solution systems.

We hypothesize that positively charged chitosan can act as sugar coatings to disperse FL-$Ti_3C_2T_x$ nanosheets with negative charges only under specific condition (proportion, mixing order and pH) and the resultant membrane fabricated by VAF of chitosan/FL-$Ti_3C_2T_x$ composite suspension can accelerate infectious wound healing. Herein, we managed to construct a stable homogeneous chitosan/FL-$Ti_3C_2T_x$ composite nanoparticles suspension system with positive charges by adjusting mixing sequence, pH, as well as the ratio of chitosan to FL-$Ti_3C_2T_x$ MXene, and subsequently prepared a multifunctional membrane with self-standing ability, good flexibility, biocompatibility, excellent photothermal antibacterial properties, and sensitive humidity response properties (Scheme 1). The construction of chitosan/FL-$Ti_3C_2T_x$ precursor suspension could allow chitosan to suture the VAF membrane together with the PVDF membrane. Additionally, the photothermal conversion ability induced by $Ti_3C_2T_x$ nanosheets could achieve further sterilization exploiting bacterial sensitively to temperature. The rat full-thickness skin tissue wound-infected model was conducted to investigate the therapeutic effect of the P-CM membrane for infectious wounds in vivo. Overall, the as-prepared P-CM membranes were expected to become a new type of wound dressings integrated with antibacterial, real-time monitoring, and pro-healing.

2. Experiment

2.1. Materials

Chitosan (molecular weight = 100,000 Da, degree of deacetylation ≥90%) was obtained from Aladdin Biochemical Technology Co., Ltd. (Shanghai, China). MAX (Ti_3AlC_2) powder was purchased from 11 Technology Co., Ltd. (Jilin China) and glacial acetic acid was purchased from Beijing chemical works (Beijing China). The PVDF filter membranes were supplied by Beijing North Tianchen Technology Co., Ltd. (Beijing, China).

2.2. Characterization

The structure of the Ti_3AlC_2 powder, FL-$Ti_3C_2T_x$ nanosheets, chitosan/FL-$Ti_3C_2T_x$ composite nanoparticles, the surface and cross-section micro topographies of the membranes were observed by scanning electron microscopy (SEM, S-4700, Hitachi, Japan) at an acceleration voltage of 20 kV. The surface elements were analyzed by energy-dispersive spectrometry (EDS, S-4700, Hitachi, Japan). Atomic force microscopy (AFM) was analyzed by Nano Scope Analysis software. The zeta potential of the suspensions and the average size of FL-$Ti_3C_2T_x$ nanosheets as well as chitosan/FL-$Ti_3C_2T_x$ nanoparticles were measured by zeta potential instrument (zetasizer Ver. 7.11, Malvern, England) at 25 °C. Each sample was tested three times (n = 3). The crystal structure of the samples was characterized using a powder diffraction of X-rays (XRD, D8 Advance, Bruker, Germany) system with Cu-Kα radiation. The relevant performance of material thermodynamics could be obtained by Thermogravimetric Analysis (TGA, Q500, TA Instruments, USA) and Derivative Thermogravimetric Analysis (DTG, Q500, TA Instruments, USA) in N_2 atmosphere.

2.3. Component analysis

The theoretical composition of the CM composite membranes can be calculated from the raw material ratio; while the practical composition can be calculated from the final residual amounts obtained by TGA data and the simultaneous Eqs. (1) and (2).

$$x + y = 1 \tag{1}$$

$$40.78\%x + y = z \tag{2}$$

where x and y represent mass percent of chitosan and FL-$Ti_3C_2T_x$ nanosheets, respectively, z represents the residual total mass of the CM membrane at 600 °C.

2.4. Synthesis of $Ti_3C_2T_x$ MXene nanosheets

$Ti_3C_2T_x$ MXene nanosheets were prepared by the method previous reported in the literature (Ghidiu et al., 2014; Wang, Zhang, et al., 2020). As shown in Scheme 1, Multilayer $Ti_3C_2T_x$ (ML-$Ti_3C_2T_x$) MXene nanosheets were obtained by selectively etching the Al layer from the precursor Ti_3AlC_2 powder with LiF/HCl solution. Specifically, 2 g of LiF

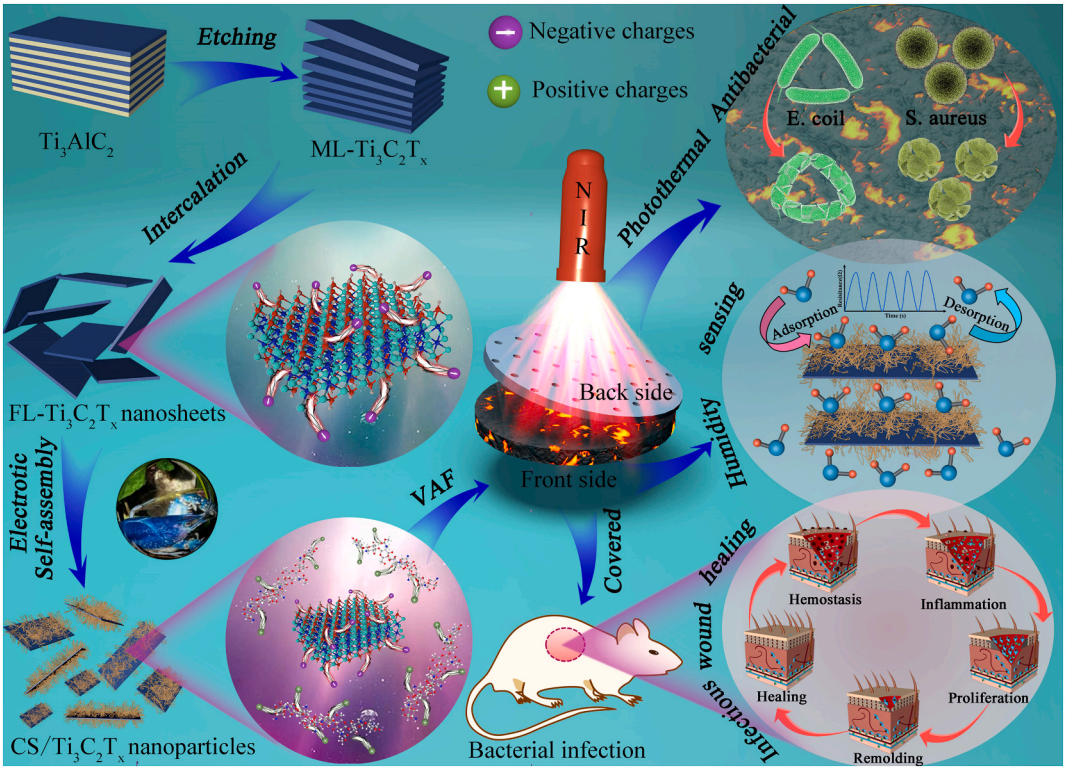

Scheme 1. Schematic illustration of the preparation of PVDF/chitosan/$Ti_3C_2T_x$ composite membrane and its application in photothermal antibacterial in vitro, humidity monitoring and infectious wound therapy in vivo.

powder was dissolved in 40 mL HCI solution (9 M) in a Teflon container and the mixture solution was magnetically stirred at a rotation of 400 rpm for 30 min. Then, 2 g of Ti_3AlC_2 powder was slowly added into the LiF/HCI solution and continuously stirred at 35 °C for 24 h to etching the Al layer. The resulting suspension was washed with deionized (DI) water and centrifuged at 3500 rpm for 10 min. The above procedure was performed repeatedly until pH > 5. Single- and/or few-layer $Ti_3C_2T_x$ (FL-$Ti_3C_2T_x$) nanosheets were prepared by the delamination of ML-$Ti_3C_2T_x$ using ethanol as intercalating agent in the experiment. Specifically, the obtained ML-$Ti_3C_2T_x$ nanosheets were dispersed in ethanol, sonicated for 1 h, and then centrifuged at 10000 rpm for 10 min. The resultant supernatant was removed and the FL-$Ti_3C_2T_x$ nanosheets were collected and redispersed in DI water. The final concentration of the prepared $Ti_3C_2T_x$ colloidal solution was determined by vacuum-assisted filtration (VAF) method according to the previous literature (Zhao et al., 2020).

2.5. Fabication of the P-M and P-CM composite membrane

The P-M composite membrane was prepared by directly filtering the FL-$Ti_3C_2T_x$ colloidal solution (20 mL, 1 mg/mL) through a PVDF membrane (diameter of 50 mm and pore size of 0.47 μm). As for the P-CM composite membrane, the specific preparation procedure was shown below: firstly, 10 mg/mL of acetic acid solution of chitosan was prepared by dissolving 1 g chitosan into 100 mL acetic acid aqueous solution (1 wt %), subsequently, the configured chitosan acetic acid aqueous solution as well as the obtained $Ti_3C_2T_x$ colloidal solution was simultaneously diluted to 1 mg/mL followed by mixing and stirring at room temperature (RT) for 6 h at different ratio; finally, the mixed suspension (20 mL) with different ratios was made into membranes using the VAF method. After drying under vacuum at RT, the resultant P-CM was immersed into DI water (water was replaced every 6 h) for 24 h to wash impurities and then stored under nitrogen atmosphere for further use.

2.6. Calculation of photothermal conversion efficiency (η)

Following Ropar's report (Roper et al., 2007), for the whole system, the energy balance can be expressed as:

$$\sum_i m_i C_{P,i} \frac{dT}{dt} = Q_{FL-Ti_3C_2T_x} + Q_{Dis} - Q_{surr} \quad (3)$$

where m and C_p represent the mass and the heat capacity of the solvent, $\frac{dT}{dt}$ represents the heating rate of the suspension, $Q_{FL-Ti3C2Tx}$ and Q_{Dis} represent the energy input from the FL-$Ti_3C_2T_x$ nanosheets and the sample cell, Q_{surr} represents the energy away from the system surface by air.

$Q_{FL-Ti_3C_2T_x}$ and Q_{surr} can be further expressed as:

$$Q_{FL-Ti_3C_2T_x} = I\left(1 - 10^{-A_{808nm}}\right)\eta \quad (4)$$

$$Q_{surr} = hs(T - T_{Surr}) \quad (5)$$

where I represents the incident laser power, A_{808nm} represents the absorbance of FL-$Ti_3C_2T_x$ nanosheets at 808 NIR irradiation, η represents the photothermal conversion efficiency, h represents heat transfer coefficient, s represents surface area, T_{surr} represents the ambient temperature.

When the whole system is in balance:

$$Q_{Ti_3C_2T_x} + Q_{Dis} - Q_{surr} = 0 \quad (6)$$

Therefore, through formula (1), (2), and (3), η can be expressed as:

$$\eta = \frac{hs(T_{Max} - T_{Surr}) - Q_{Dis}}{I\left(1 - 10^{-A_{808\ nm}}\right)} \quad (7)$$

where T_{Max} represents equilibrium temperature. In the above expression, only hs is unknown for calculating η. Dimensional driving force temperature (θ) and sample system time constant (τ_s) are defined to

solve the value of *hs*. θ and τ_s can be expressed as:

$$\theta = \frac{T - T_{Surr}}{T_{Max} - T_{Surr}} \tag{8}$$

$$\tau_s = \frac{\sum_i m_i C_{p,i}}{hs} \tag{9}$$

Simultaneous Eqs. (1), (6), and (7) can be obtained:

$$\frac{d\theta}{dt} = \frac{1}{\tau_s}\left(\frac{Q_{Ti_3C_2T_x} + Q_{Dis}}{hs(T_{Max} - T_{Surr})} - \theta\right) \tag{10}$$

When the incident laser stops irradiating, the system goes into the cooling stage, at which time we can get that $Q_{Ti3C2Tx} + Q_{Dis} = 0$. Therefore, Eq. (8) can be simplified as:

$$\frac{d\theta}{dt} = -\frac{1}{\tau_s}\theta \tag{11}$$

Integrating the above formula:

$$t = -\tau_s Ln^{\theta} \tag{12}$$

2.7. Preparation of bacterial cells

The antibacterial tests were performed according to standard antibacterial protocols. Gram-negative *E. coli* and gram-positive *S. aureus* were selected as the representative bacterial species to estimate the antibacterial activity of different membranes in our tests (S. Wu et al., 2019). Cells (both *E. coli* and *S. aureus*) were cultured in sterile Luria-Bertani (LB) medium at 37 °C for 24 h and then harvested by centrifugation at 3000 rpm for 5 min. Bacterial cells were washed five times with 2 mL normal saline to remove soluble contaminants. The concentrations of final bacterial suspensions of *E. coli* and *S. aureus* were both 1×10^9 CFU·mL^{-1}.

2.8. Antibacterial activity tests in vitro

Before use, the concentrations of *E. coli* and *S. aureus* suspension were diluted into 1×10^7 CFU·mL^{-1} and all the samples were sterilized by ultraviolet irradiation for 30 min. The pure PVDF membrane, P-M composite membrane (back side) and P-CM_2 (back side) composite membrane were divided into two groups, one with NIR light applied (NIR (−) groups) while the other without NIR light applied (NIR (+) groups). The specific experimental steps are as follows: Firstly, the membranes (d = 15 mm) were placed in the bottom of 24-well plate and then 1 mL of bacterial suspension (1×10^7 CFU·mL^{-1}) was dropped onto the back surface of the sterilized membranes followed by treated with or without 808 nm NIR vertical irradiation (1 W. cm^{-2}) for 10 min. After incubation at 37 °C for 6 h, the 24-well plate as well as the membrane was washed thoroughly with 9 mL of 0.9% (w/v) saline solution followed by diluted 100 times. Then, 100 μL of the diluted bacterial suspension was spread evenly onto the LB agar plates and incubated at 37 °C for 24 h. Each group was repeated for 2 times and each time used two LB agar plates to culture bacteria. The photographs of bacterial colonies were recorded using a camera and the relative bacterial viability (RBV) was calculated by the equation (Liu et al., 2020):

$$RBV\ (\%) = \frac{N_t}{N_c} \times 100\% \tag{13}$$

where N_t and N_c represent the number of bacterial colonies formed in the experiment groups and in the blank control group (pure PVDF membrane without 808 nm NIR irradiation), respectively.

2.9. Humidity response characterization

As shown in Fig. 5C, a set of homemade assembled setups was used to evaluate the humidity response of the prepared P-CM membrane in this work. When tested, the P-CM membrane (d = 12 mm) was placed onto a similarly sized silicone sheet and connected at both ends using wires with spring clamps. The digital multimeter was used to monitor the changes of resistance, and the humidity chamber was used to control humidity. Humidity levels varied in the RH range of 30%–90%. 30% and 50% RH were selected as baseline humidity. The sensitivity was calculated as follows (Choi et al., 2018):

$$S = (R_H - R_0)/R_0 \times 100\% = \Delta R/R_0 \times 100\% \tag{14}$$

The resistance at different humidity was tested three times (n = 3).

2.10. Wound healing tests in vivo

Sprague Dawley (SD) rats (200–220 g) were obtained from SBF Biotechnology Co., Ltd. (Beijing, China) and housed centrally in cages prior to surgery. According to different treated methods, the SD rats were randomly divided into two groups with three SD rats in each group (n = 3). The P-CM_2 membrane group irradiated by NIR light (808 nm) was selected as the experimental group while the PVDF membrane group irradiated by NIR light (808 nm) was selected as the blank control group. Before surgery, all the SD rats were intraperitoneally anesthetized with chloral hydrate (10%). Subsequently, a round wound of 10 mm diameter was created on the back of the SD rats using a scalpel and a press cell mold (d = 10 mm). Then 20 μL of the *S. aureus* suspensions (1×10^8 CFU/mL) was injected into and smeared on the wound to cause infection using pipette. A piece of membrane (d = 12 mm) was applied onto the infected wound. After 30 min, 808 nm NIR light (0.6 W. cm^{-2}) was vertical irradiation irradiated for 5 min. The photographs of the process of wound healing were taken using a camera at different time intervals (0, 3, 7, and 14 days). To further investigate the healing effect of each group, the skin sections after 14 days were collected and stained with hematoxylin-eosin (H&E) to conduct histological examination.

All the animal experiments were conducted in strict accordance with the National Institutes of Health Guide for the Care and Use of Laboratory Animals (NIH Publications No. 8023, revised 1978) and approved by the animal ethics committee of Beijing Anzhen Hospital, Capital Medical university.

2.11. Statistical analysis

In our experiments, one-way analysis of variance (ANOVA) was performed to compare the statistical significance of the differences in results. All results were expressed as mean ± standard deviation.

3. Results and discussion

3.1. Stability of FL-$Ti_3C_2T_x$ MXene and chitosan/$Ti_3C_2T_x$ nanocomposite particles under different conditions

As depicted in Scheme 1, FL-$Ti_3C_2T_x$ MXene nanosheets were prepared by the means of selectively etching the Al layer with LiF/HCl mixed solution followed by ethanol intercalation. Due to the etching of the Al layer and the intercalation of ethanol, the peak of (104) almost disappeared and the peak of (002) went a leftward shift from 9.5° to 6.94° suggesting that the interlayer spacing increased by 3.42 Å (as shown in XRD pattern, Fig. S1).

The stability of FL-$Ti_3C_2T_x$ MXene suspensions at different pH was first assessed qualitatively by observing whether agglomeration and/or sedimentation occurred over time (Fig. S2). At the initial time, FL-$Ti_3C_2T_x$ nanosheets at all pH values maintained stable state without agglomeration and/or sedimentation (Fig. S2, first line). Subsequently, FL-$Ti_3C_2T_x$ nanosheets in suspension at pH 3, 4, 12 began to agglomerate and settle, indicating an unstable state. It should be noted that the agglomeration and/or sedimentation rate of FL-$Ti_3C_2T_x$ nanosheets in the suspension of pH = 3 was faster than that in suspension of pH = 4,

which suggested a higher pH value was conducive to the stability of FL-$Ti_3C_2T_x$ nanosheets under acidic conditions. The stability of FL-$Ti_3C_2T_x$ nanosheets at different pH was then evaluated by zeta potential that was an important index to characterize the stability of colloidal dispersion system. A larger absolute value of zeta potential suggested a more stable state. As shown in Fig. S3, the absolute value of zeta potential of FL-$Ti_3C_2T_x$ nanosheets suspensions showed a gradually increasing trend with increasing pH, which was generally consistent with the changing trend from pH = 3 to pH = 11 presented in Fig. S2. As for FL-$Ti_3C_2T_x$ nanosheets suspension at pH = 12, we found that a distinct white rather than black precipitate appeared at the bottom of the bottle at last, suggesting that the FL-$Ti_3C_2T_x$ nanosheets had been oxidized in the strongly alkaline condition. Therefore, the appearance of sedimentation and/or aggregation phenomena at pH = 12 can be explained by the fact of the oxidization of FL-$Ti_3C_2T_x$ nanosheets.

The dispersion stability of chitosan/FL-$Ti_3C_2T_x$ composite nanoparticles in solution was further investigated. As shown in Fig. 1A, chitosan/FL-$Ti_3C_2T_x$ composite nanoparticles was able to be stably dispersed in the pH range of 3–6 solution and no agglomeration and/or sedimentation occurred within 120 h. In contrast, the chitosan/FL-$Ti_3C_2T_x$ composite nanoparticles became extremely unstable in the pH range of 7–12, and the dispersions agglomerated and settled at a rate visible to the naked eye at the initial time. Furthermore, the rate of agglomeration and/or sedimentation was approximately positively related to the magnitude of the pH. Zeta potentials of chitosan/FL-$Ti_3C_2T_x$ composite nanoparticles suspensions at pH 3–7 were measured and displayed in Fig. 1B. As the increase of pH, the values of zeta potential decreased gradually, indicating that these composite nanoparticles became more and more unstable in solution. The above phenomenon that show in Fig. 1A and B can be summarized as: the system of chitosan/FL-$Ti_3C_2T_x$ composite nanoparticles suspensions are stable in acidic environment, but unstable in neutral or alkaline environment, which is different from that of pure FL-$Ti_3C_2T_x$ nanosheets suspensions. Due to hydrogen and electrostatic attraction, chitosan chains and FL-$Ti_3C_2T_x$ nanosheets can combine with each other to form positively charged chitosan/FL-$Ti_3C_2T_x$ composite nanoparticles. Compared with pure FL-$Ti_3C_2T_x$ nanosheets, chitosan/FL-$Ti_3C_2T_x$ nanoparticles exhibited a larger average size (Fig. 1C) and opposite charges, which in turn precisely confirmed the formation of composite nanoparticles. It has been reported that chitosan is responsive to pH due to the presence of amine groups (—NH_2) (Ladet et al., 2008). When pH < pKa, chitosan chains can dissolve in aqueous solution as a

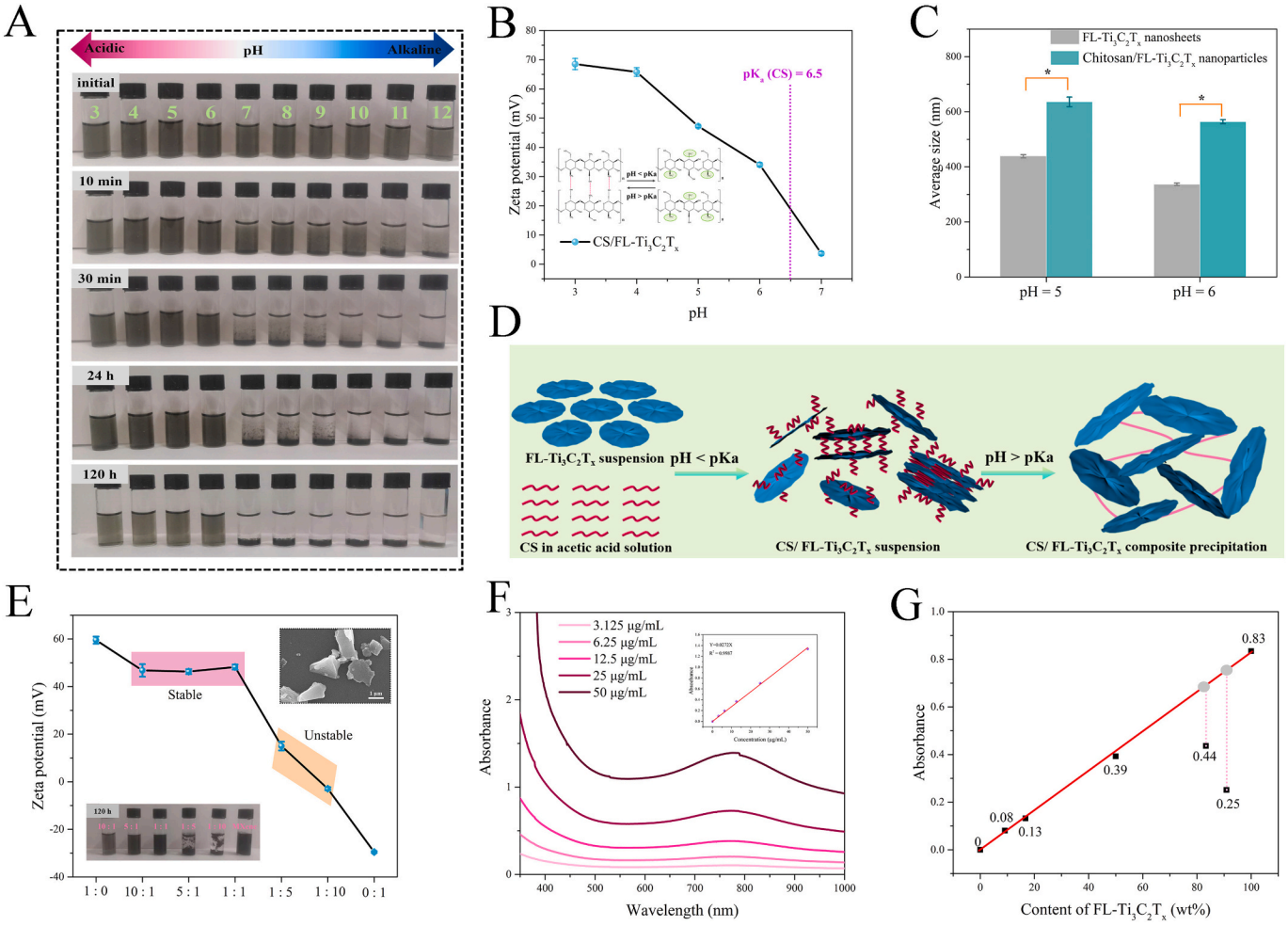

Fig. 1. (A) The photographs of state of chitosan/FL-$Ti_3C_2T_x$ (10:1) composite nanoparticle suspensions at different time (0 min, 10 min, 30 min, 24 h, 120 h) and different pH (3−12). (B) Zeta potential of chitosan/FL-$Ti_3C_2T_x$ composite nanoparticle suspensions (10:1) at different pH values (3–7). (C) Average size of FL-$Ti_3C_2T_x$ nanosheets and chitosan/FL-$Ti_3C_2T_x$ (10:1) nanoparticles at pH 5 and 6. The inset is the molecular structural formula of chitosan when pH < pKa and pH > pKa. (D) Schematic diagram of the state of chitosan/FL-$Ti_3C_2T_x$ (10:1) nanoparticles at pH < pKa and pH > pKa. (E) Zeta potential of chitosan/FL-$Ti_3C_2T_x$ composite nanoparticle suspensions at different ratios. The inset at bottom left and top right are the optical photographs of chitosan/FL-$Ti_3C_2T_x$ suspensions at different ratios and SEM of chitosan/FL-$Ti_3C_2T_x$ nanoparticles, respectively. (F) Absorbance of FL-$Ti_3C_2T_x$ suspension at different concentration. The inset is the relationship of absorbance and concentration of FL-$Ti_3C_2T_x$ in suspension. (G) Absorbance at 808 nm of chitosan/FL-$Ti_3C_2T_x$ suspensions at different ratios. Data are reported as means ± SD (*p < 0.05).

polyelectrolyte via electrostatic repulsion; while pH > pKa, chitosan chains will entangle with each other and finally separate from the water (Yang, Bai, et al., 2018). For chitosan, the value of pKa is about 6.5. The existence of chitosan chains renders the composite nanoparticles pH-responsive. As displayed in Fig. 1D, when pH < 6.5, the composite nanoparticles can stably disperse in aqueous solution due to the electrostatic repulsion; on the contrary, when pH > 6.5, the composite nanoparticles will agglomerate and settle in a short time with the decrease of electrostatic repulsion.

Further studies found that not all proportions of chitosan/FL-$Ti_3C_2T_x$ composite nanoparticles could maintain stability at pH < pKa. We investigated the stability of chitosan/FL-$Ti_3C_2T_x$ suspensions at five proportions (10:1, 5:1, 1:1, 1:5, and 1:10) and found only at high proportions (10:1, 5:1, and 1:1) could the system be stabilized. As displayed in Fig. S4 and Fig. 1E, the chitosan/FL-$Ti_3C_2T_x$ suspensions at the proportions of 10: 1, 5:1 as well as 1:1 were able to be stable within 120 h, and the absolute values of corresponding zeta potentials were also large (47.23 mV ± 0.41, 46.70 mV ± 1.05, and 47.6 mV ± 1.47, respectively); in contrast, the chitosan/FL-$Ti_3C_2T_x$ suspensions at the proportions of 1:5 and 1:10 performed extremely unstable state, manifested by rapid agglomeration and/or sedimentation, and the corresponding zeta potentials were only 17.3 mV ± 0.96 and 3.17 mV ± 0.70, respectively. The above experimental results show that to maintain a stable dispersion state, it is necessary to ensure that there is enough chitosan at the initial stage in the mixed suspension, so the mixing sequence is very important. If it is the dropwise addition of chitosan solution into the FL-$Ti_3C_2T_x$ MXene suspension, the amount of chitosan at the initial state is completely insufficient to maintain the stability of the whole mixed system, thus leading to agglomeration and sedimentation in a short time. As shown in Fig. S5, at the same pH (pH = 5) and the same proportion (1:1), the bottle labeled A was able to show a stable dispersion, whereas the bottle labeled B was not. The microtopography of chitosan/FL-$Ti_3C_2T_x$ composite nanoparticles was showed in Fig. 1E. Different from the two-dimensional layered structure of FL-$Ti_3C_2T_x$ nanosheets, chitosan/FL-$Ti_3C_2T_x$ complex exhibited an irregular three-dimensional bulk structure. According to Lambert-Beer law, absorbance is directly proportional to the concentration of the absorbing substance. With the increase of the concentration of FL-$Ti_3C_2T_x$ nanosheets, the absorbance increased gradually (Fig. 1F). At 808 nm, the absorbance of FL-$Ti_3C_2T_x$ suspension versus FL-$Ti_3C_2T_x$ concentration satisfied the line equation: Y = 0.0272X. In the chitosan/FL-$Ti_3C_2T_x$ suspension, the light absorbing substance is still FL-$Ti_3C_2T_x$. However, the absorbance of chitosan/FL-

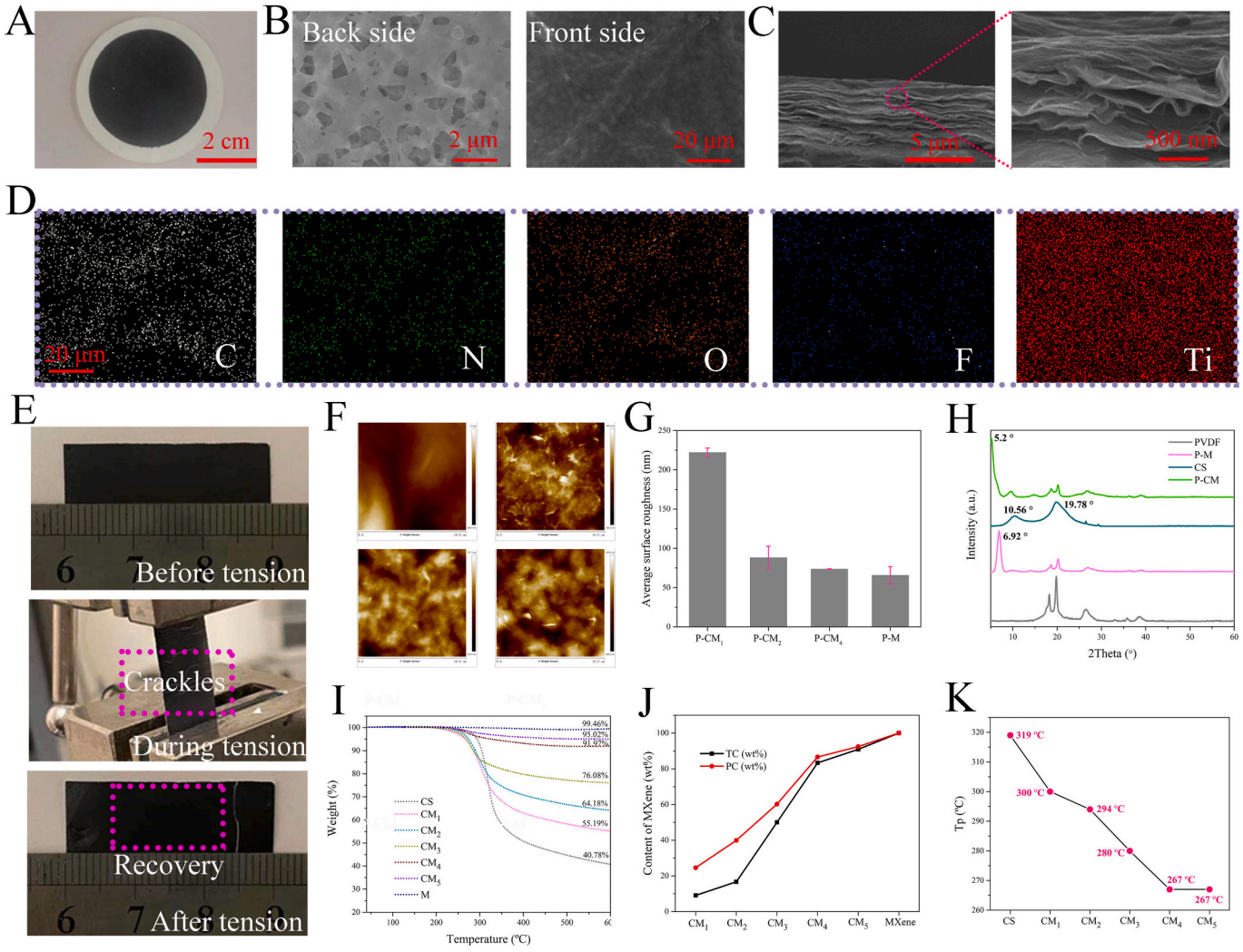

Fig. 2. (A) Optical image of the as-prepared P-CM_2 membrane. (B) SEM image of the back side and the front side of the P-CM_2 membrane. (C) SEM images of longitudinal section of the P-CM_2 membrane at different magnifications. (D) EDS elemental mappings of the graph (C). (E) optical images of the P-CM_2 membrane before tension, during tension, and after tension. (F) AFM images of different membranes. (G) Ra of different membranes. (H) XRD patterns of chitosan powder, PVDF, P-M, and P-CM membranes. (I) TGA curves of M membrane, chitosan powder and different CM membranes in N_2 atmosphere. (J) TC values and PC values of FL-$Ti_3C_2T_x$ in different CM membranes. (K) T_p of different membranes.

$Ti_3C_2T_x$ suspension versus FL-$Ti_3C_2T_x$ concentration did not satisfy the linear relationship at 808 nm due to the formation of precipitation of chitosan/FL-$Ti_3C_2T_x$ composite nanoparticles (Fig. S6 and Fig. 1G).

3.2. Preparation and characterization of the P-M and P-CM membranes

As shown in Fig. S7, pure PVDF membrane exhibited a porous surface and profile structure with an average diameter of 0.47 μm. The channel structure of PVDF membrane itself can allow light to reach the other side of the membrane through one side. After VAF, FL-$Ti_3C_2T_x$ nanosheets and chitosan/FL-$Ti_3C_2T_x$ composite nanoparticles were deposited onto the surface of PVDF using chitosan as molecular needles, forming a functional coating (Fig. 2A). We named the membrane including the flexible substrate PVDF as P-M and/or P-CM. The upper portion of the composite membrane is called M and/or CM. The microtopography of the back side and front side of the P-CM_2 membrane was identified by SEM. The back side still exhibited a porous structure while the front side showed a relatively compact structure (Fig. 2B). Additionally, the P-CM_2 membrane formed by chitosan/FL-$Ti_3C_2T_x$ composite nanoparticles via VAF still had obvious layered structure (Fig. 2C), which is in consistent with the structure of other pure MXene membranes prepared by VAF that reported in the literature previously (Ling et al., 2014; Shahzad et al., 2016). The EDS elemental mapping results of the front side of P-CM_2 revealed the uniform distribution of C, N, O, F, and Ti elements (Fig. 2D), demonstrating chitosan acted as sugar coatings covered the surface of FL-$Ti_3C_2T_x$ MXene by electrostatic attraction, hydrogen bonding and van der Waals force. Due to the introduction of rigid chain network of chitosan, chitosan-based membranes with otherwise weak mechanical properties are extremely prone to fracture when subjected to deformation such as stretching, bending, and twisting, which can hardly meet the demand of practical applications. When PVDF was used as the basement membrane, it could effectively solve the above problem caused by the deformation of CM membrane. As shown in Fig. 2E, the upper layer, CM_2 membrane layer, was still easy to rupture. However, after withdrawal of the external force, the CM_2 membrane would quickly recover with the recovery of the basement membrane, thus guaranteeing the overall integrity of the membrane. The planar topology of the membranes was detected by AFM. From the results of Fig. 2F and G, the average surface roughness (Ra) of P-CM membrane was higher than that of P-M membrane and the Ra value increased with the increase of chitosan content, which indicated that the nanocomposite particles were easier to form relatively rough surface than MXene nanosheets. It should be noted that rough surface is more conducive to capture bacteria and improve the antibacterial ability of the whole material (Liu et al., 2021).

Due to the intercalation effect of positively charged chitosan, the interlayer spacing (also known as the d-spacing) of MXene nanosheets in the P-CM composite membrane was enlarged from 1.27 nm to 1.70 nm compared with the M membrane, which appearing as a left shift (from 6.92° to 5.2°) of the (002) peak on the XRD patterns (Fig. 2H). Moreover, the peak at 10.56° and 19.78° that originally related to the crystallization of chitosan disappeared in the P-CM membrane, implying that the presence of FL-$Ti_3C_2T_x$ nanosheets could hinder the ordered recrystallization of chitosan. Based on the final residue amounts obtained by pyrolysis of M membrane, chitosan powder, as well as different CM membranes and according to the simultaneous Eqs. (1) and (2), the practical composition of different CM membranes can be easily determined from the TGA curves (Fig. 2I). For neat M membrane, the final residual mass percentage was 99.46%. The trace amount of mass loss may be due to the bound water present in the FL-$Ti_3C_2T_x$ nanosheets. However, the final residual mass percentage of chitosan powder was only 40.78%, suggesting that a large of amount of substance was pyrolyzed and burned away. As depicted in Fig. 2J, as the FL-$Ti_3C_2T_x$ content in the chitosan/FL-$Ti_3C_2T_x$ precursor suspension increased, the practical content (PC) and theoretical content (TC) of FL-$Ti_3C_2T_x$ in CM membranes increased at the same time. However, there was always a difference that decreased with the increasing content of FL-$Ti_3C_2T_x$ between PC and TC, which indicating that there always existed a part of chitosan that cannot combine with FL-$Ti_3C_2T_x$. Additionally, the pyrolysis temperature (T_p) exhibited an obvious decreasing trend with increasing FL-$Ti_3C_2T_x$ content or decreasing chitosan content (Fig. S8 and Fig. 2K).

3.3. Photothermal effect under different conditions

As previously mentioned, as well as reported in the literature (Xu et al., 2020), FL-$Ti_3C_2T_x$ MXene has a wide range of UV–Vis absorption spectra, implying the great potential for photothermal conversion. The photothermal performance of FL-$Ti_3C_2T_x$ nanosheets was evaluated under 808 nm laser irradiation, a biological light source and favorable for biomedical applications. As shown in Figs. S9, S10, S11 and S12, the temperature elevation of FL-$Ti_3C_2T_x$ nanosheets was positively correlated with the concentration of FL-$Ti_3C_2T_x$ nanosheets, irradiation time, and power density (light intensity), which is consistent with that reported in the literature (Xuan et al., 2016). Compared with pure water, suspension temperature containing FL-$Ti_3C_2T_x$ nanosheets showed a rapid increased trend even at a lower concentration (such as 8, 16, 32 μg/mL), indicating that FL-$Ti_3C_2T_x$ nanosheets had a high efficiency of photothermal conversion. The photothermal stability of the FL-$Ti_3C_2T_x$ nanosheets was further evaluated by recording the heating and cooling curves of FL-$Ti_3C_2T_x$ suspension recurrently. As can be seen from the results of Fig. S13, the performance of the photothermal effect of FL-$Ti_3C_2T_x$ nanosheets is highly reproducible. After five cycles, the temperature of the suspension was still able to reach more than 60 °C. The photothermal conversion efficiency η of the as-prepared FL-$Ti_3C_2T_x$ nanosheets was calculated based on the data of Fig. S14, Fig. S15, and the equation of (5). The value of η of the as-prepared FL-$Ti_3C_2T_x$ nanosheets was 29.4%, which is higher than that of Au nanorods (21%), bismuth sulfide hollow microspheres (23.8%), and Cu_9S_5 NCs (25.7%) and so on (Lin et al., 2017; Liu et al., 2020; Liu et al., 2014; Zeng et al., 2013). The photothermal performance of chitosan/FL-$Ti_3C_2T_x$ nanocomposite particles was also evaluated. Benefitting from the photothermal conversion ability of FL-$Ti_3C_2T_x$ nanosheets, all ratios of suspensions (chitosan: FL-$Ti_3C_2T_x$ = 10:1, 5:1, 1:1, 1:5, 1:10) exhibited a trend of increasing temperature with increasing lighting time (Fig. 3A and S16). In the several sets of stable system with high zeta potential (such as chitosan: FL-$Ti_3C_2T_x$ = 10:1, 5:1, 1:1), ΔT increased with increasing FL-$Ti_3C_2T_x$ nanosheets content. Moreover, for the stable system (such as chitosan: FL-$Ti_3C_2T_x$ = 5:1), the value of ΔT still increased with the increase of power density at the same irradiation time (Fig. 3B and S17), and the nanocomposite suspension also exhibited good cycle stability (Fig. S18). However, as the FL-$Ti_3C_2T_x$ content continued to increase, the ΔT values instead became smaller (chitosan: FL-$Ti_3C_2T_x$ = 1:5, 1:10). It was worth noting that the 1:10 ratio of suspension heated at the fastest rate yet had the lowest ΔT value, which resulted from the rapid sedimentation of the unstable chitosan/FL-$Ti_3C_2T_x$ nanocomposite particles in the system.

The P-CM composite membranes were believed to have good photothermal conversion potential due to the introduction of FL-$Ti_3C_2T_x$ nanosheets. Therefore, the photothermal effect performance of the composite membranes were also investigated. P-CM_2 (both the back side and the front side) was selected to assess the photothermal performance. As shown in Fig. 3C and D, pure PVDF membrane could not convert light energy to heat energy whether in air and in water, as indicated by the basically unchanged temperature during the irradiation with 808 nm NIR. In contrast, P-CM_2 could easily improve its temperature through photothermal conversion. However, it exhibited different photothermal response characteristics in water and in air. In detail, the photothermal response of the P-CM_2 in air was almost instantaneous, which could be called “point response”. When the 808 nm NIR hit the surface of the P-CM_2 membrane, the center of the membrane would reach the maximum temperature in seconds. As for in water, the photothermal response of

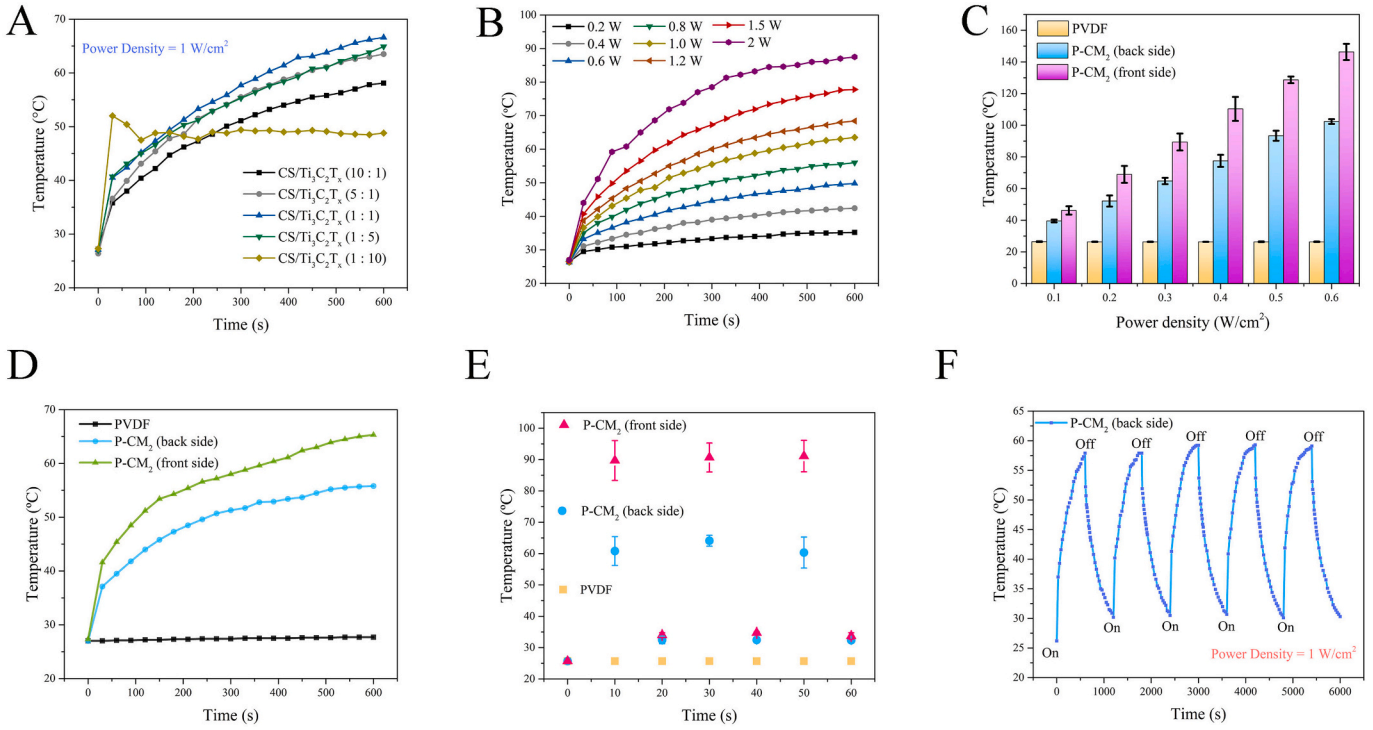

Fig. 3. (A) Time-dependent temperature increase curves of chitosan/FL-$Ti_3C_2T_x$ nanocomposite suspensions at different ratios, and (B) different power density. (C) The highest temperature of different membrane surface under NIR laser irradiation at different power density in air. (D) Time-dependent temperature increase curves of different membranes in water. (E) Recycling heating/cooling point of different membranes in air. (F) Recycling heating/cooling curve of different membranes in water.

the P-CM_2 was a "linear response". With the extension of irradiation time, the surface temperature of the P-CM_2 membrane increased gradually, while the heating rate slowed down gradually, the phenomenon of which was the same as that in chitosan/FL-$Ti_3C_2T_x$ nanoparticle suspension. Additionally, compared with directly irradiating the front side of the P-CM_2 membrane, when the light was irradiated to the back side, the value of ΔT as well as the heating rate would obviously decrease whether in air and in water. To further assess the photothermal stability of the P-CM_2 membrane, the recycling temperature variations of P-CM_2 membrane were recorded under heating with an NIR laser radiation for 10 s (in air) or 10 min (in water) followed by natural cooling to room temperature for three (in air) and five (in water) laser on/off cycles. As depicted in Fig. 3E, F, and S19, no significant deterioration was found during the cycling process, indicating a durable photothermal performance of the P-CM_2 membrane whether in air or water. The difference in the photothermal response characteristics of the membrane in water and in air was due to the specific heat capacity of medium. The specific heat capacity of water made up of water molecules was 4.2 kJ. kg^{-1}. K^{-1}, while that of air consisting of nitrogen and oxygen molecules was 1.4 kJ. kg^{-1}. K^{-1} (Fig. S20). Therefore, under the same heat production conditions, the membrane in air had faster heating rate and larger ΔT value.

3.4. Antibacterial activity in vitro

Material-contact-guided bacteriostasis and antibiotics-delivery method are two common antimicrobial strategies. Compared with the latter, the former exhibits higher safety and more lasting antibacterial activity (Zheng, Tong, et al., 2021). The introduction of chitosan and the excellent and stable photothermal conversion performance inspired us to explore the antibacterial activity of the P-CM membrane. *E. coli* and *S. aureus* were selected as the model systems against gram-negative and gram-positive bacteria, respectively. Plate counting method was used to evaluate the antibacterial activity of different samples.

As shown in Fig. 4A and B, PVDF + NIR irradiation exhibited negligible antibacterial activity against both two bacteria. In contrast, P-M + NIR irradiation and P-CM_2 + NIR irradiation possessed the most significant antibacterial effect, with nearly 100% bactericidal efficiency compared with the blank control group (PVDF without NIR irradiation group), whether it was for gram-negative bacteria *E. coli* or gram-positive bacteria *S. aureus*. That was to say the P-M and P-CM_2 exhibited basically consistent and excellent antibacterial activity under 808 nm laser irradiation. In practical applications, samples will be contaminated with external bacteria at any time. However, limited by various factors, the P-CM_2 membrane cannot be irradiated by 808 nm NIR all the time, so it is also significant to explore long-time antibacterial performance of the membrane under no NIR irradiation condition. As depicted in Fig. 4B, the relative bacterial viability (*E. coli* and *S. aureus*) of the P-CM_2 group containing chitosan decreased from 67.5% and 57.0% to 11.2% and 19.2% compared with the P-M group without chitosan, respectively, which implied that the P-CM_2 membrane had the long-term antibacterial property due to the presence of chitosan.

SEM images of *E. coli* and *S. aureus* were recorded to evaluate the micromorphological changes of bacteria under different treatments. As illustrated in Fig. 4C, both *E. coli* and *S. aureus* treated by PVDF membrane with or without NIR irradiation and P-M membrane without NIR irradiation exhibited intact cell morphologies and smooth cell membrane, indicating a negligible damage. However, when treated with P-CM_2 membrane without NIR irradiation, some of the bacteria began to deform, such as surface ruffling or cell rupture, whereas others continue to maintain relatively intact cell morphology as well as smooth cell membrane surfaces. After irradiation with 808 nm NIR, many of the P-M and P-CM_2 treated bacteria exhibited amorphous morphologies and disrupted structures, indicating a significant serious damage and an excellent antibacterial effect. The results of antibacterial activities of different membranes observed from the SEM images were in good agreement with those of plate counting method showed in Fig. 4A and B. All the findings prove that the P-CM_2 possessed a long-term and highly effective antibacterial activity and can be used as wound dressings for

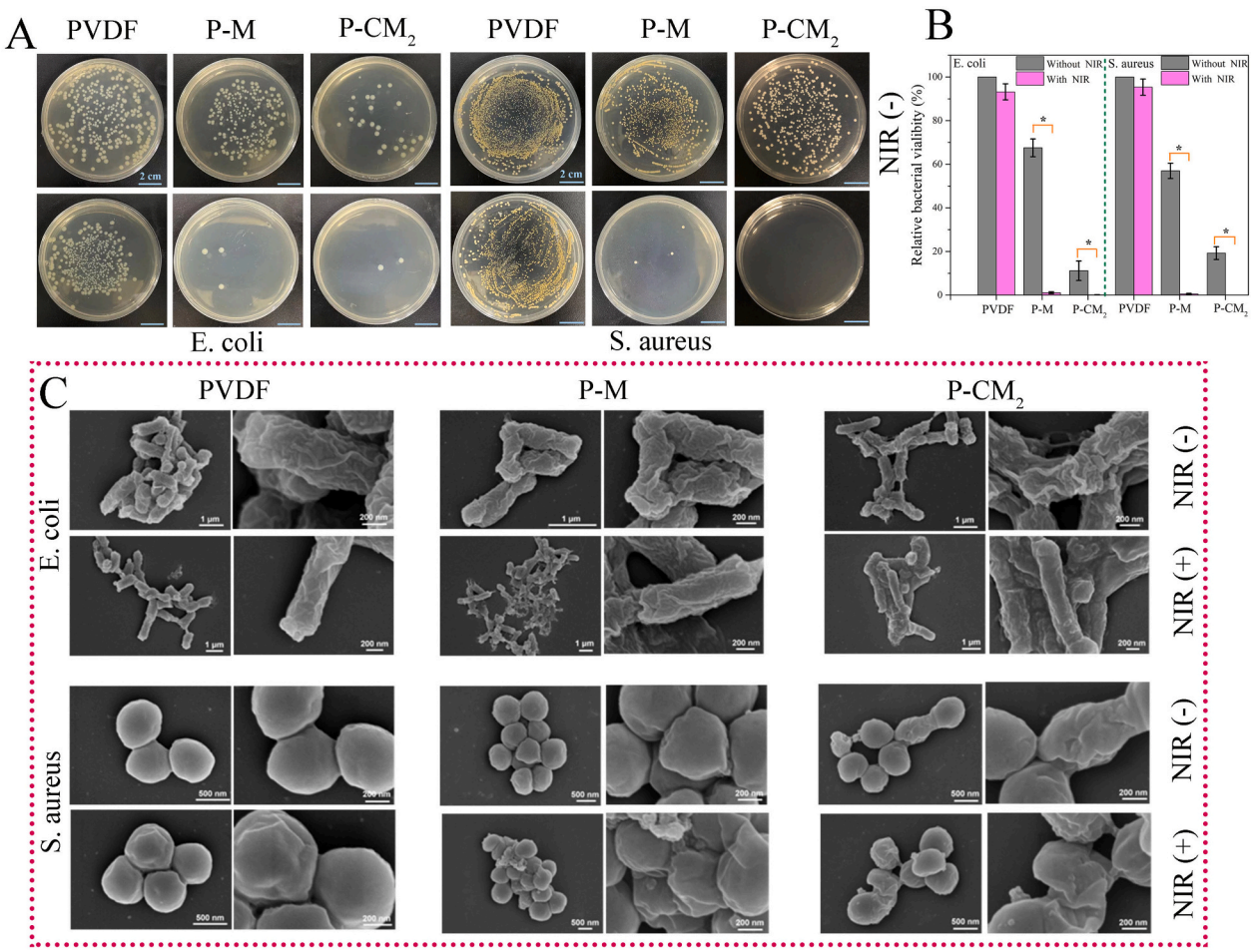

Fig. 4. (A) Photographs of bacterial colonies of *E. coli* (left) and *S. aureus* (right) treated with or without 808 nm NIR irradiation. (B) Relative bacterial viability of different groups determined by plate counting method. (C) SEM images of *E. coli* (above) and *S. aureus* (below) of different groups. Data are reported as means ± SD (*$p < 0.05$).

infectious wound treatment.

3.5. Wettability and humidity response

Given that moist environment is more conducive to wound healing and recovery than dry environment (Chen et al., 2018), it is of importance to construct a hydrophilic surface for wound dressings. As shown in Fig. 5A and B, PVDF-supported pure FL-$Ti_3C_2T_x$ MXene layer (back side of the P-M membrane) possessed a hydrophilic surface (≈50°) due to the existence of the hydrophilic functional groups (such as —OH, —O, and —F) on the surface of FL-$Ti_3C_2T_x$ MXene nanosheets. Comparatively, the composite membranes (P-CM_2, P-CM_3, P-CM_4, P-CM_5) showed a smaller WCA after introducing a certain proportion of chitosan into the membrane system, demonstrating a stronger wetting effect. However, the P-CM_1 composite membrane showed a larger WCA. It has been reported that the wettability can be modified by the synergistic effect between the hygroscopicity and the surface roughness of the material (Li et al., 2019). Accordingly, the increase of WCA of the P-CM_1 was possible due to the increased surface roughness caused by the excessive viscosity of the precursor suspension.

Recently, artificial sensing devices have received more and more attention (Zheng, Zhu, et al., 2021). MXenes have been reported that it can change the electrical resistance through pathways of interlayer spacing caused by adsorption and desorption of water molecules to achieve humidity responsive sensing (Muckley et al., 2017; Muckley et al., 2018). Therefore, the P-CM membrane might be able to monitor the changes of humidity around the wound during the healing process. A set of homemade assembled setups consisting of digital multimeter and humidity chamber was employed to explore the humidity response of the prepared P-CM membrane in this work (Fig. 5C). The resistance of different membranes was firstly measured at a fixed relative humidity (RH = 50%). As expected, the resistance of the membranes increased with the increase of chitosan content (Fig. 5D). The P-CM_2 membrane was selected to evaluate the sensitivity of humidity sensor due to its best wettability among the P-CM membranes. As depicted in Fig. 5E, the values of $\Delta R/R_0$ exhibited a continuous increase with the increase of RH for a wide range of 30%–90%. The real-time monitoring of RH from 50% to 60%, 70%, 80%, and 90% was conducted. As shown in Fig. 5F, clear differences were observed in the output signal of the resistor as the humidity interval varied. In addition, Multicycle humidity response tests were also performed to prove the stability and reproducibility of the resistance signals. The four curves all exhibited stable and repeatable resistance changes in cyclic testing and as the humidity interval increased, the values of $\Delta R/R_0$ became larger, indicating a better response (Fig. 5G). The effect of temperature on the P-CM_2 membrane was also studied. It was found that the resistance of the membrane changed slightly in the temperature range of 25 °C ~ 65 °C (Fig. 5H). In summary, as a wound dressing, the P-CM_2 composite membrane can not only maintain the relatively moist environment of the wound, but also monitor the change of humidity of the surrounding environment, which provides the best strategy for rapid wound healing.

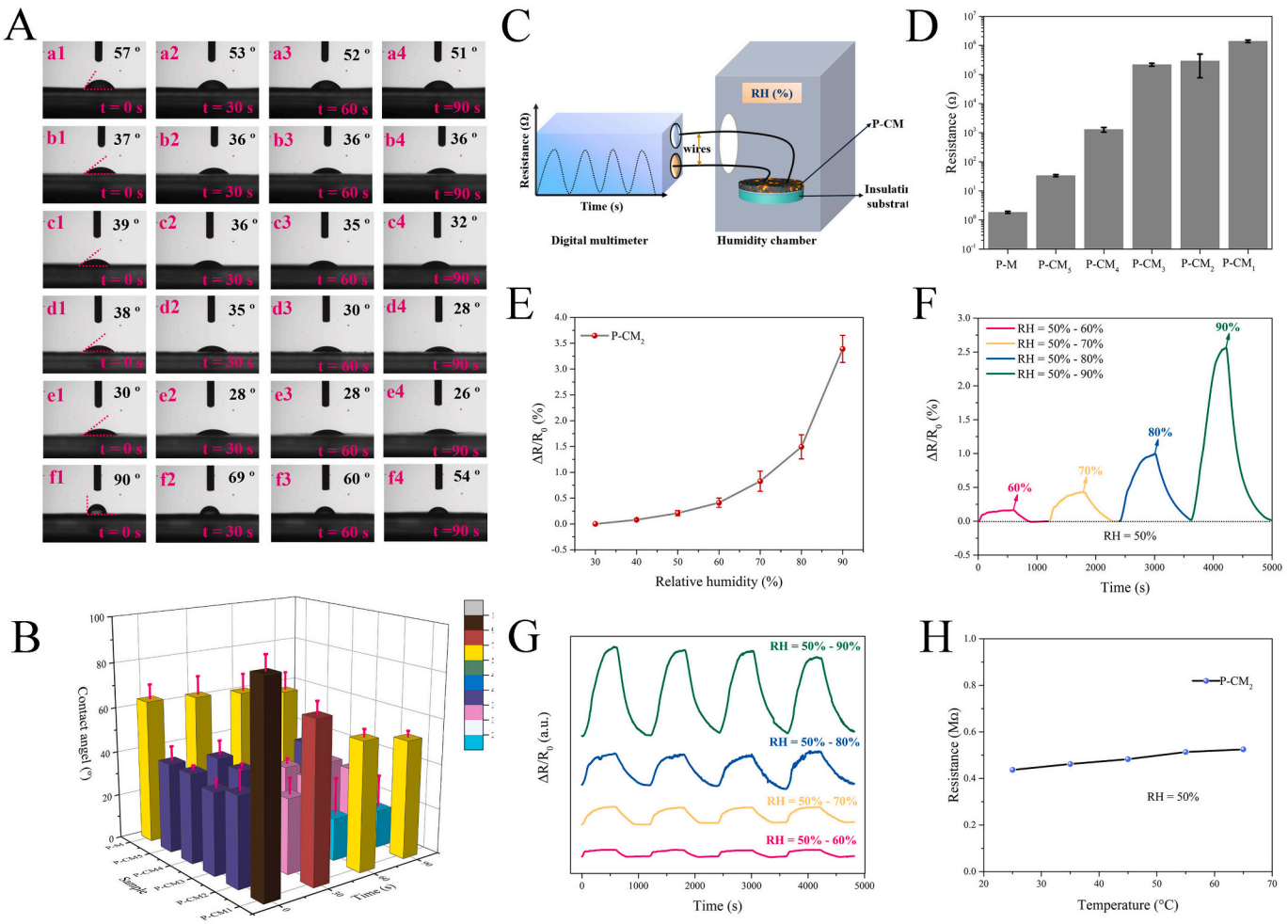

Fig. 5. (A) WCAs of different samples at 0, 30, 60, and 90 s (From bottom to up are P-CM_1, P-CM_2, P-CM_3, P-CM_4, P-CM_5 membranes, and P-M membrane). (B) The histogram of the WCA values of different membranes at different time pointes (0, 30, 60, 90 s). (C) Real-time humidity response test schematic diagram of the humidity sensing device. (D) Resistance of different membranes. (E) $\Delta R/R_0$ – RH curve of the P-CM_2 membrane (RH = 30%–90%). (F) Humidity response tests of the with P-CM_2 membrane increasing RH. (G) Multicycle humidity response tests with P-CM_2 membrane under different humidity changes. (H) Resistance changes of P-CM_2 at different temperatures with a fixed RH (50%).

3.6. Infectious wound healing evaluation in vivo

On the one hand, the ingenious design of double-layered P-CM_2 membrane enables the light to pass through the channels originally existed inside the PVDF membrane to the other side of the membrane, thus achieving photothermal conversion; On the other hand, the long-term and high-efficiency antibacterial properties endow the membrane with great potential in promoting wound healing, especially for bacterial infection wounds. Therefore, we hypothesized that if the front facet formed by the chitosan/FL-$Ti_3C_2T_x$ composite nanoparticles was directly covered on the infectious wounds, the P-CM_2 membrane was expected to achieve rapid healing of infectious wounds with the help of the antibacterial activity originating from chitosan and photothermal effect. To assess the therapeutic effect of the P-CM_2 composite membrane on infectious wound in vivo, a rat full-thickness skin tissue wound-infected model was constructed using *S. aureus* at a concentration of 10^8 CFU/mL to simulate infectious wound (Fig. 6A). The wound healing efficiencies of the P-CM_2 membrane group and the blank control group were evaluated by observing wound surface topography, calculating wound area, and analyzing wound histological results. During irradiation with 808 nm NIR light (0.6 W/cm^2), the temperature at the wound center covered with the composite membrane P-CM_2 could be always maintained at about 50 °C–55 °C by adjusting the distance between the laser emitter and the wound (Fig. 6B), which illustrated the potential of the composite membrane serving as the photothermal therapeutic agent to increase the local temperature, eventually killing the bacteria around the wound and promoting wound healing.

In the process of wound healing, a shrinking wound can act as a barrier to the skin and protect the wound from the invasion of microorganisms (Zhang, Yao, et al., 2020). As displayed in Fig. 6C and D, the wounds both showed a gradually decreasing and shrinking trend with time in each group. However, the healing rate of wounds in the P-CM_2 treated group was significantly faster than that in the PVDF group at either period (day 3, 7, 14). Moreover, the wounds in the PVDF group even appeared purulent due to the infectious wound. The calculated residual wound area presented in Fig. 6E quantitatively proved that the P-CM_2 had a significant therapeutic effect in infectious wound healing compared with the PVDF group. Specifically, the wound healing ratio reached 51.33 ± 8.37%, 84.49 ± 3.53%, and 95.82 ± 0.90% at day 3, 7, 14 in the P-CM_2 treated group, but only13.9 ± 2.46%, 65.96 ± 4.21%, and 89.09 ± 1.31% in the PVDF group (Fig. S21), which indicated a quicker reepithelialization process in the P-CM_2 treated group due to its antibacterial activity and healing promoting effect. To further investigate the microscope therapeutic effect of the P-CM_2 membrane on the infectious wound, the wound histological results were further analyzed (Fig. 6C). Skin tissues were harvested at day 14 and stained with hematoxylin and eosin (H&E). Compared with the PVDF group, the P-CM_2 group exhibited a better state of skin recovery evidenced by continuous

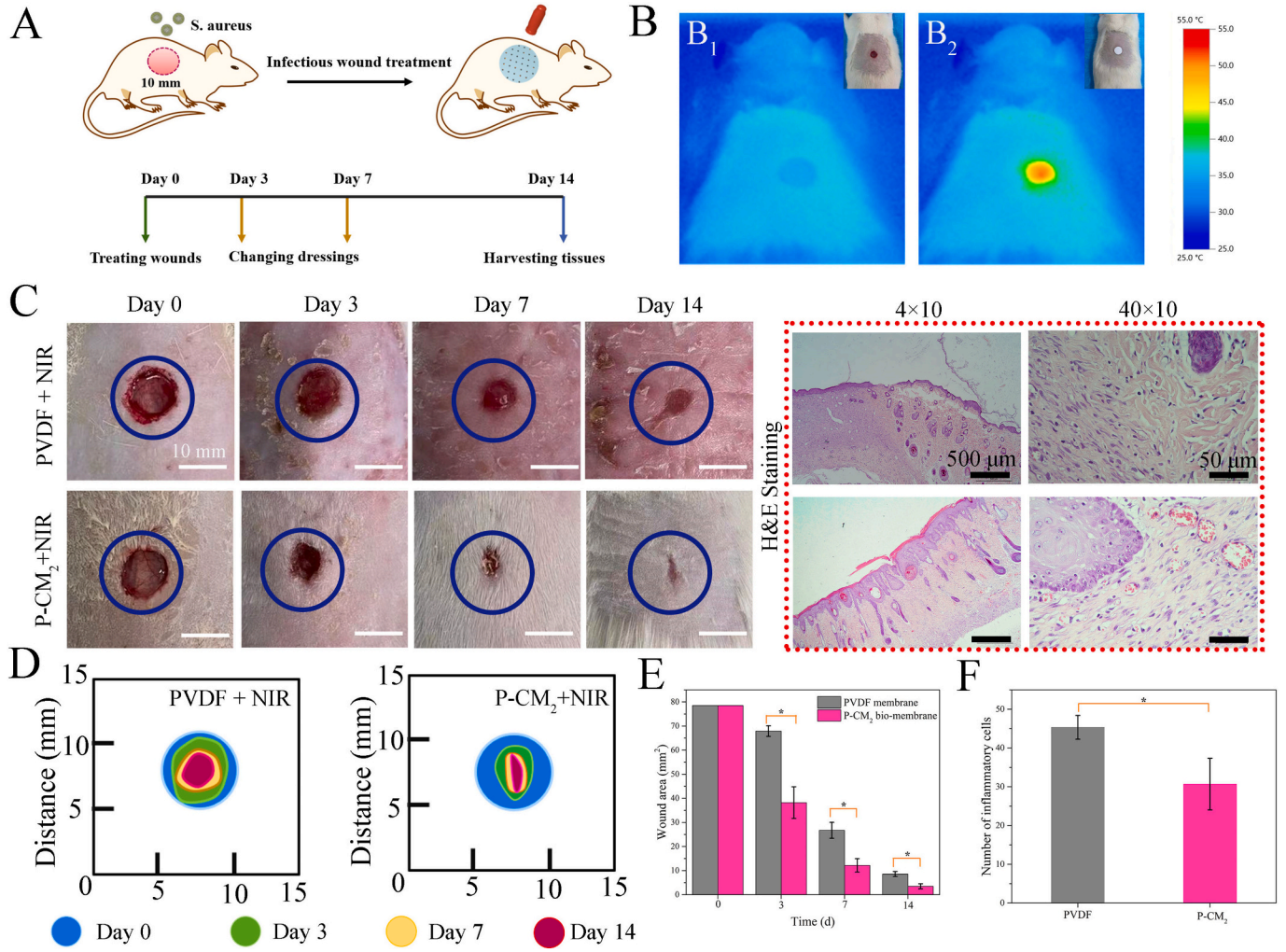

Fig. 6. (A) Schematic of rat wounds and treatment protocol. (B) Photographs of photothermal treatment of rats. (C) Representative photographs of wounds infected with *S. aureus* and treated with different methods from Day 0 to Day 14 and the corresponding H&E staining of wound tissues on Day 14. (D) Schematic of wound healing from Day 0 to Day 14. (E) Quantitative wound area statistics from Day 0 to Day 14. Data are reported as means ± SD (*p < 0.05).

and coherent epidermis tissues, ordered dermis, well-organized granulation tissue, and complete and mature hair follicle structure, all of which were important indicators for better wound healing (Li et al., 2020). Additionally, obvious inflammatory cells were observed in the PVDF group, suggesting the serious bacterial infection. In contrast, relatively few inflammation cells could be found in the P-CM_2 group (Fig. 6F). Generally, the histological results were consistent with the trend of wound healing observed in optical photographs. All the results showed that P-CM_2 membrane could cure bacterial infection wounds and promote the healing and regeneration of skin tissue. We chose rats belonging to rodents as a model for theoretical studies of wound healing. Rodent experimental models can reflect the pro-healing ability of dressings to some extent. However, rodent healing is mainly through wound contraction, whereas human healing is mainly through reepithelialization. Therefore, there are still certain limitations to using rodents as a model for wound healing. To further investigate the potential of P-CM membranes for clinical translation, we will employ a more closely related animal model (e.g. pigs) to the human kindred for more precise experimental results in subsequent experiments.

4. Conclusion

In summary, positively charged chitosan could disperse $Ti_3C_2T_x$ nanosheets and formed a stable chitosan/$Ti_3C_2T_x$ composite suspension that further acted as precursor solution for preparing multifunctional membranes with good wettability (WCA ≈ 20°–30°), excellent flexibility, photothermal conversion ability, and high-efficiency antibacterial activity to accelerate infectious wound healing. The results of zeta potential and SEM images proved that chitosan was encapsulated on the surface of $Ti_3C_2T_x$ nanosheets as a sugar coating by electrostatic attraction, which converts the $Ti_3C_2T_x$ nanosheet surface from negative to positive charge and stably disperses in aqueous acetic acid solution. Meanwhile, chitosan covered on $Ti_3C_2T_x$ nanosheets prevented direct contact of the nanosheets with wound tissue, thus minimizing side reactions in photothermal therapy. The as-prepared P-CM membranes could be folded, stretched freely without breaking up and falling off and exhibited nearly 100% bactericidal efficiency both against *E. coli* and *S. aureus*, making it a highly ideal flexible wound dressing for infectious wound treatment. In the rat full-thickness skin tissue wound-infected test, the wound healing rate can be accelerated by 37.4%, 18.52% and 5.8% in the treated experimental group compared with the control group. In addition, the highly sensitive and reproducible humidity responsive property enables the membranes with real-time and on-site monitoring of ambient humidity around the wound site, which can provide help for future smart wound care.

CRediT authorship contribution statement

Liangyu Wang: Data curation, Methodology, Investigation, Writing – original draft. **Lin Du:** Methodology, Validation. **Mengmeng Wang:** Software, Validation. **Xing Wang:** Resources, Validation. **Saihua Tian:** Visualization. **Yan Chen:** Software. **Xiaoyue Wang:** Resources, Validation. **Jie Zhang:** Resources, Validation. **Jun Nie:** Supervision. **Guiping Ma:** Conceptualization, Project administration, Funding acquisition, Supervision, Writing – review & editing, Resources.

Declaration of competing interest

The authors declare that they have no known competing financial interests or personal relationships that could have appeared to influence the work reported in this paper.

Acknowledgements

This work was supported by the National Natural Science Foundation of China (Grant No. 51973009).

Appendix A. Supplementary data

Supplementary data to this article can be found online at https://doi.org/10.1016/j.carbpol.2022.119209.

References

Brown, E. D., & Wright, G. D. (2016). Antibacterial drug discovery in the resistance era. *Nature, 529*(7586), 336–343.
Chen, G., Yu, Y., Wu, X., Wang, G., Ren, J., & Zhao, Y. (2018). Bioinspired multifunctional hybrid hydrogel promotes wound healing. *Advanced Functional Materials, 28*(33).
Choi, S. J., Yu, H., Jang, J. S., Kim, M. H., Kim, S. J., Jeong, H. S., & Kim, I. D. (2018). Nitrogen-doped single graphene fiber with platinum water dissociation catalyst for wearable humidity sensor. *Small, 14*(13), Article e1703934.
Dong, Y., Shi, H., & Wu, Z. S. (2020). Recent advances and promise of MXene-based nanostructures for high-performance metal ion batteries. *Advanced Functional Materials, 30*(47).
Ghidiu, M., Lukatskaya, M. R., Zhao, M. Q., Gogotsi, Y., & Barsoum, M. W. (2014). Conductive two-dimensional titanium carbide 'clay' with high volumetric capacitance. *Nature, 516*(7529), 78–81.
Gupta, A., Mumtaz, S., Li, C. H., Hussain, I., & Rotello, V. M. (2019). Combatting antibiotic-resistant bacteria using nanomaterials. *Chemical Society Reviews, 48*(2), 415–427.
Han, X., Huang, J., Lin, H., Wang, Z., Li, P., & Chen, Y. (2018). 2D ultrathin MXene-based drug-delivery nanoplatform for synergistic photothermal ablation and chemotherapy of cancer. *Advanced Healthcare Materials, 7*(9), Article e1701394.
Jiang, Q., Luo, B., Wu, Z., Gu, B., Xu, C., Li, X., & Wang, X. (2021). Corn stalk/AgNPs modified chitin composite hemostatic sponge with high absorbency, rapid shape recovery and promoting wound healing ability. *Chemical Engineering Journal, 421*.
Jiang, X., Kuklin, A. V., Baev, A., Ge, Y., Ågren, H., Zhang, H., & Prasad, P. N. (2020). Two-dimensional MXenes: From morphological to optical, electric, and magnetic properties and applications. *Physics Reports, 848*, 1–58.
Jin, L., Guo, X., Gao, D., Wu, C., Hu, B., Tan, G., & Zhang, X. (2021). NIR-responsive MXene nanobelts for wound healing. *NPG Asia Materials, 13*(1).
Jones, K. E., Patel, N. G., Levy, M. A., Storeygard, A., Balk, D., Gittleman, J. L., & Daszak, P. (2008). Global trends in emerging infectious diseases. *Nature, 451*(7181), 990–993.
Ladet, S., David, L., & Domard, A. (2008). Multi-membrane hydrogels. *Nature, 452* (7183), 76–79.
Li, M., Liang, Y., He, J., Zhang, H., & Guo, B. (2020). Two-pronged strategy of biomechanically active and biochemically multifunctional hydrogel wound dressing to accelerate wound closure and wound healing. *Chemistry of Materials, 32*(23), 9937–9953.
Li, Y., Cui, X., Zhao, M., Xu, Y., Chen, L., Cao, Z., & Wang, Y. (2019). Facile preparation of a robust porous photothermal membrane with antibacterial activity for efficient solar-driven interfacial water evaporation. *Journal of Materials Chemistry A, 7*(2), 704–710.
Liang, Y., Zhao, X., Hu, T., Chen, B., Yin, Z., Ma, P. X., & Guo, B. (2019). Adhesive hemostatic conducting injectable composite hydrogels with sustained drug release and photothermal antibacterial activity to promote full-thickness skin regeneration during wound healing. *Small, 15*(12), Article e1900046.
Lin, H., Wang, X., Yu, L., Chen, Y., & Shi, J. (2017). Two-dimensional ultrathin MXene ceramic nanosheets for photothermal conversion. *Nano Letters, 17*(1), 384–391.
Lin, H., Wang, Y., Gao, S., Chen, Y., & Shi, J. (2018). Theranostic 2D tantalum carbide (MXene). *Advanced Materials, 30*(4).
Ling, Z., Ren, C. E., Zhao, M. Q., Yang, J., Giammarco, J. M., Qiu, J., & Gogotsi, Y. (2014). Flexible and conductive MXene films and nanocomposites with high capacitance. *Proceedings of the National Academy of Sciences of the United States of America, 111*(47), 16676–16681.
Liu, T., Wang, C., Gu, X., Gong, H., Cheng, L., Shi, X., & Liu, Z. (2014). Drug delivery with PEGylated MoS2 nano-sheets for combined photothermal and chemotherapy of cancer. *Advanced Materials, 26*(21), 3433–3440.
Liu, Y., Xiao, Y., Cao, Y., Guo, Z., Li, F., & Wang, L. (2020). Construction of chitosan-based hydrogel incorporated with antimonene nanosheets for rapid capture and elimination of bacteria. *Advanced Functional Materials, 30*(35).
Liu, Z., Zhao, X., Yu, B., Zhao, N., Zhang, C., & Xu, F. J. (2021). Rough carbon-iron oxide nanohybrids for near-infrared-II light-responsive synergistic antibacterial therapy. *ACS Nano, 15*(4), 7482–7490.
Lord, M. S., Cheng, B., McCarthy, S. J., Jung, M., & Whitelock, J. M. (2011). The modulation of platelet adhesion and activation by chitosan through plasma and extracellular matrix proteins. *Biomaterials, 32*(28), 6655–6662.
Luo, X., Zhu, L., Wang, Y.-C., Li, J., Nie, J., & Wang, Z. L. (2021). A flexible multifunctional triboelectric nanogenerator based on MXene/PVA hydrogel. *Advanced Functional Materials, 31*(38), 2104928.
Ma, X., Wu, G., Dai, F., Li, D., Li, H., Zhang, L., & Deng, H. (2021). Chitosan/polydopamine layer by layer self-assembled silk fibroin nanofibers for biomedical applications. *Carbohydrate Polymers, 251*, Article 117058.
Maleski, K., Mochalin, V. N., & Gogotsi, Y. (2017). Dispersions of two-dimensional titanium carbide MXene in organic solvents. *Chemistry of Materials, 29*(4), 1632–1640.
Muckley, E. S., Naguib, M., & Ivanov, I. N. (2018). Multi-modal, ultrasensitive, wide-range humidity sensing with Ti3C2 film. *Nanoscale, 10*(46), 21689–21695.
Muckley, E. S., Naguib, M., Wang, H. W., Vlcek, L., Osti, N. C., Sacci, R. L., & Ivanov, I. N. (2017). Multimodality of structural, electrical, and gravimetric responses of intercalated MXenes to water. *ACS Nano, 11*(11), 11118–11126.
Panda, S., Rout, T. K., Prusty, A. D., Ajayan, P. M., & Nayak, S. (2018). Electron transfer directed antibacterial properties of graphene oxide on metals. *Advanced Materials, 30* (7).
Rasool, K., Helal, M., Ali, A., Ren, C. E., Gogotsi, Y., & Mahmoud, K. A. (2016). Antibacterial activity of Ti(3)C(2)Tx MXene. *ACS Nano, 10*(3), 3674–3684.
Ren, J., Yin, X., Chen, Y., Chen, Y., Su, H., Wang, K., & Zhang, C. (2020). Alginate hydrogel-coated syringe needles for rapid haemostasis of vessel and viscera puncture. *Biomaterials, 249*, Article 120019.
Roper, D. K., Ahn, W., & Hoepfner, M. (2007). Microscale heat transfer transduced by surface plasmon resonant gold nanoparticles. *The Journal of Physical Chemistry C, 111* (9), 3636–3641.
Shahzad, F., Alhabeb, M., Hatter Christine, B., Anasori, B., Man Hong, S., Koo Chong, M., & Gogotsi, Y. (2016). Electromagnetic interference shielding with 2D transition metal carbides (MXenes). *Science, 353*(6304), 1137–1140.
Shao, M., Fan, Y., Zhang, K., Hu, Y., & Xu, F.-J. (2021). One nanosystem with potent antibacterial and gene-delivery performances accelerates infected wound healing. *Nano Today, 39*.
Tao, N., Zhang, D., Li, X., Lou, D., Sun, X., Wei, C., & Liu, Y. N. (2019). Near-infrared light-responsive hydrogels via peroxide-decorated MXene-initiated polymerization. *Chemical Science, 10*(46), 10765–10771.
Wang, C., Niu, H., Ma, X., Hong, H., Yuan, Y., & Liu, C. (2019). Bioinspired, injectable, quaternized hydroxyethyl cellulose composite hydrogel coordinated by mesocellular silica foam for rapid, noncompressible hemostasis and wound healing. *ACS Applied Materials & Interfaces, 11*(38), 34595–34608.
Wang, J., Zhang, Z., Zhu, J., Tian, M., Zheng, S., Wang, F., & Wang, L. (2020). Ion sieving by a two-dimensional Ti3C2Tx alginate lamellar membrane with stable interlayer spacing. *Nature Communications, 11*(1), 3540.
Wang, L., Zhong, Y., Qian, C., Yang, D., Nie, J., & Ma, G. (2020). A natural polymer-based porous sponge with capillary-mimicking microchannels for rapid hemostasis. *Acta Biomaterialia, 114*, 193–205.
Wu, F., Zheng, H., Wang, W., Wu, Q., Zhang, Q., Guo, J., & Hong, W. (2020). Rapid eradication of antibiotic-resistant bacteria and biofilms by MXene and near-infrared light through photothermal ablation. *Science China Materials, 64*(3), 748–758.
Wu, S., Li, A., Zhao, X., Zhang, C., Yu, B., Zhao, N., & Xu, F. J. (2019). Silica-coated gold-silver nanocages as photothermal antibacterial agents for combined anti-infective therapy. *ACS Applied Materials & Interfaces, 11*(19), 17177–17183.
Xin, Q., Shah, H., Nawaz, A., Xie, W., Akram, M. Z., Batool, A., & Gong, J. R. (2019). Antibacterial carbon-based nanomaterials. *Advanced Materials, 31*(45), Article e1804838.
Xu, D., Li, Z., Li, L., & Wang, J. (2020). Insights into the photothermal conversion of 2D MXene nanomaterials: Synthesis, mechanism, and applications. *Advanced Functional Materials, 30*(47).
Xu, Q., Guo, L., A, S., Gao, Y., Zhou, D., Greiser, U., & Wang, W. (2018). Injectable hyperbranched poly(beta-amino ester) hydrogels with on-demand degradation profiles to match wound healing processes. *9*(8), 2179–2187.
Xu, Z., Liu, G., Ye, H., Jin, W., & Cui, Z. (2018). Two-dimensional MXene incorporated chitosan mixed-matrix membranes for efficient solvent dehydration. *Journal of Membrane Science, 563*, 625–632.
Xuan, J., Wang, Z., Chen, Y., Liang, D., Cheng, L., Yang, X., & Geng, F. (2016). Organic-Base-driven intercalation and delamination for the production of functionalized titanium carbide nanosheets with superior photothermal therapeutic performance. *Angewandte Chemie International Edition, 55*(47), 14569–14574.
Yang, J., Bai, R., & Suo, Z. (2018). Topological adhesion of wet materials. *Advanced Materials, 30*(25), Article e1800671.

Yang, Q., Wang, Y., Li, X., Li, H., Wang, Z., Tang, Z., & Zhi, C. (2018). Recent Progress of MXene-based nanomaterials in flexible energy storage and electronic devices. *Energy & Environmental Materials, 1*(4), 183–195.

Zeng, J., Goldfeld, D., & Xia, Y. (2013). A plasmon-assisted optofluidic (PAOF) system for measuring the photothermal conversion efficiencies of gold nanostructures and controlling an electrical switch. *Angewandte Chemie (International Ed. in English), 52*(15), 4169–4173.

Zhang, W., Pan, Z.-Z., Lv, W., Lv, R., Shen, W., Kang, F., & Huang, Z.-H. (2019). Wasp nest-imitated assembly of elastic rGO/p-Ti3C2Tx MXene-cellulose nanofibers for high-performance sodium-ion batteries. *Carbon, 153*, 625–633.

Zhang, X., Yao, D., Zhao, W., Zhang, R., Yu, B., Ma, G., & Xu, F. J. (2020). Engineering platelet-rich plasma based dual-network hydrogel as a bioactive wound dressing with potential clinical translational value. *Advanced Functional Materials, 31*(8).

Zhang, Y., Cheng, W., Tian, W., Lu, J., Song, L., Liew, K. M., & Hu, Y. (2020). Nacre-inspired tunable electromagnetic interference shielding Sandwich films with superior mechanical and fire-resistant protective performance. *ACS Applied Materials & Interfaces, 12*(5), 6371–6382.

Zhao, X., Guo, B., Wu, H., Liang, Y., & Ma, P. X. (2018). Injectable antibacterial conductive nanocomposite cryogels with rapid shape recovery for noncompressible hemorrhage and wound healing. *Nature Communications, 9*(1), 2784.

Zhao, X., Wang, L.-Y., Tang, C.-Y., Zha, X.-J., Liu, Y., Su, B.-H., & Yang, W. (2020). Smart Ti3C2Tx MXene fabric with fast humidity response and joule heating for healthcare and medical therapy applications. *ACS Nano, 14*(7), 8793–8805.

Zheng, K., Tong, Y., Zhang, S., He, R., Xiao, L., Iqbal, Z., & Li, Y. (2021). Flexible bicolorimetric polyacrylamide/chitosan hydrogels for smart real-time monitoring and promotion of wound healing. *Advanced Functional Materials, 31*(34). https://doi.org/10.1002/adfm.202102599

Zheng, L., Zhu, M., Wu, B., Li, Z., Sun, S., & Wu, P. (2021). Conductance-stable liquid metal sheath-core microfibers for stretchy smart fabrics and self-powered sensing. Science. *Advances, 7*(22), eabg4041.